Tunable spin photogalvanic effect in two-dimensional van der Waals ferroelectric semiconductors with spin-orbit coupling

Shibo Fang ●,[1] Min Wang ●,[1,2] Xingyue Yang ●,[1] Zongmeng Yang,[1] Qiuhui Li,[1] Zhaochu Luo,[1,*] and Jing Lu[1,3,4,5,6,7,†]

[1]*State Key Laboratory of Artificial Microstructure and Mesoscopic Physics, School of Physics,*
Peking University, Beijing 100871, People's Republic of China

[2]*School of Information Science and Engineering, Hebei University of Science and Technology,*
Shijiazhuang, 050018, People's Republic of China

[3]*Collaborative Innovation Center of Quantum Matter, Beijing 100871, People's Republic of China*

[4]*Beijing Key Laboratory for Magnetoelectric Materials and Devices (BKL-MEMD),*
Peking University, Beijing 100871, People's Republic of China

[5]*Peking University Yangtze Delta Institute of Optoelectronics, Nantong 226010, People's Republic of China*

[6]*Key Laboratory for the Physics and Chemistry of Nanodevices, Peking University, Beijing 100871, People's Republic of China*

[7]*Beijing Key Laboratory of Quantum Devices, Peking University, Beijing 100871, People's Republic of China*

Spin photogalvanic effect is a nonlinear effect that can generate spin currents through optical excitation in intrinsic semiconductors without parity inversion symmetry. The efficient control of the spin photogalvanic effect is of great significance for the research of computing-in-memory devices. In this work, we investigate the ferroelectric modulation of the spin photogalvanic effect in two-dimensional (2D) van der Waals (vdW) ferroelectric semiconductors with spin-orbit coupling, including the in-plane, out-of-plane, and in-plane/out-of-plane-coupled ferroelectrics. We provide the general form of the spin photogalvanic effect controlled by ferroelectricity in 2D vdW spin-orbit coupling ferroelectric semiconductors by the second-order perturbation theory. In the in-plane ferroelectrics excited by circularly polarized light, we discover an effect where the reversal of the ferroelectric polarization will maintain the spin current unchanged but change the direction of the charge current. We name this effect the hidden spin current modulation. Using first-principles quantum transport simulation, we validate our theory with three cases of the black phosphorus-like Bi (in-plane ferroelectric), monolayer α-GeTe (out-of-plane ferroelectric), and α-In$_2$Se$_3$ (in-plane and out-of-plane coupled ferroelectric). Our study paves the way for the research of next-generation low-dimensional computing-in-memory devices.

I. INTRODUCTION

The spin photogalvanic effect (SPGE) refers to a phenomenon where spin currents are generated by illuminating intrinsic semiconductors without spatial inversion symmetry [1,2]. This effect was named and extended from the photogalvanic effect [2,3]. Similar to the photogalvanic effect, SPGE also arises from the second-order perturbation of the dipole electron-light interaction and relates to the band topology [4,5]. However, unlike the photogalvanic effect, which focuses on the charge current, SPGE focuses on spin currents and it requires the presence of the spin-momentum locking [6,7]. To the best of our knowledge, the spin-momentum locking effects can be classified into two categories: the relativistic type and the nonrelativistic type. The former includes the Rashba effect and the Dresselhaus effect, where the spin splittings originate from the high-speed motion of electrons in the Wannier orbit [8,9]. The latter includes the conventional ferromagnetic systems [10–12] and the antiferromagnetic systems that do not possess the *PT*-symmetry (parity-time), such as the

altermagnets [13,14] and the noncoplanar antiferromagnets [15]. Furthermore, if we only consider the local characteristics of the *PT*-symmetric antiferromagnets, there is also an interesting phenomenon called the "hidden spin polarization" [16–18]. Recently, an interesting development is that in the antiferromagnetic systems with *PT* symmetry but broken *P* and *T* symmetries, the system can generate a pure spin current by spin photogalvanic effect due to the hidden spin polarization [7,19].

In recent years, the spin-orbit coupling effect has become a focal point in condensed matter physics [20]. From the perspective of material preparation, the existence of spin-orbit coupling enables the long-range magnetic ordering at the thermodynamic level in magnetic two-dimensional (2D) materials such as the CrI$_3$, CrPS$_4$, and Fe$_x$GeTe$_2$ family ($x = 3$, 4, and 5) [21–24]. For the theoretical research, spin-orbit coupling plays a crucial role in the strong correlation effects [25], topological band theory [26], valleytronics [27], and macroscopic topological structures [28]. For example, a recent intriguing study revealed that in certain strongly correlated systems such as transition metal compounds with 3*d* orbitals, the spin-orbit coupling splitting would be enhanced by the strong on-site Coulomb correlation, thereby enabling the realization of designing strong effective spin-orbit

*Corresponding author: zhaochu.luo@pku.edu.cn
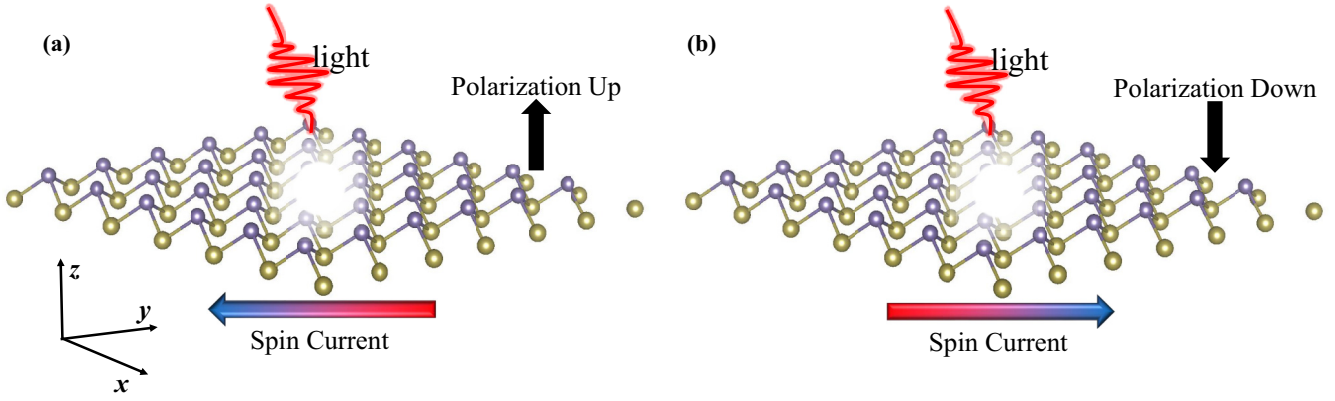†Corresponding author: jinglu@pku.edu.cn

FIG. 1. Schematic illustration of the ferroelectric-controlled spin photogalvanic effect in van der Waals ferroelectric materials with spin orbit coupling. (a) and (b) correspond to the different ferroelectric polarization states.

coupling materials composed of light elements [25]. From the applied perspective, the spin-orbit coupling encompasses the electricity and magnetism, holding great potential for manipulating magnetic states via electricity [20]. For instance, the spin transistors [29], which have the potential to become the next generation of logic devices, and spin-orbit torques [30], which have already become the next generation of magnetic storage devices, heavily rely on the assistance of spin-orbit coupling. As for the light-matter interaction, spin-orbit coupling (SOC) also plays an indispensable role. For example, the Rashba effect is considered to be one of the reasons for the long lifetime of photo-generated charge carriers in perovskite photovoltaic materials [31,32].

Recently, the successful preparation of the van der Waals (vdW) ferroelectric materials has injected tremendous vitality into the development of the novel ferroelectric devices [33,34]. Due to the atomically flat interfaces in vdW ferroelectric materials, they overcome the issue of ferroelectricity suppression at extremely low scales caused by the interface effects in traditional perovskite ferroelectrics [35]. This makes vdW ferroelectric materials highly suitable as raw materials for the next generation of ultrathin ferroelectric devices with novel properties [36,37]. For example, the ferroelectric diodes fabricated from the monolayer vdW ferroelectric α-In$_2$Se$_3$ and vdW metal NbX$_2$ ($X =$ S, Se, and Te) are predicted to exhibit symmetric and highly-responsive bidirectional tunable photocurrent, providing an ideal solution for the study of the artificial visual neural synapses [38].

The nonvolatile control of the spin photogalvanic effect is of great significance for the research of combing the information storage and computing functionalities [6]. Combining ferroelectricity with spin-orbit coupling is the most direct approach to achieve nonvolatile charge-spin conversion [39]. However, there is currently no systematic study on this issue. Here, we have chosen to study the aforementioned issues in 2D vdW ferroelectric systems for the following reasons: (1) With the miniaturization of memory sizes, traditional bulk perovskite materials are no longer suitable for continued use as ferroelectric memories [35], and there is still debate regarding the mechanisms of the doped HfO$_2$-based ferroelectric materials [40]. Two-dimensional ferroelectric materials are currently considered ideal materials due to their

well-understood mechanisms and atomically-thin ferroelectricity [37]. (2) The relativistic effects in 3D crystal systems are too complex, while relativistic effects in 2D systems are relatively simple [20,41].

In this work, we investigate the ferroelectric modulation of the spin photogalvanic effect in in 2D vdW ferroelectric semiconductors with spin-orbit coupling, including the in-plane, out-of-plane, and in-plane/out-of-plane-coupled ferroelectrics, as shown in Fig. 1 and Table I. We provide the general form of the spin photogalvanic effect controlled by ferroelectricity in 2D vdW spin-orbit coupling ferroelectric semiconductors by second-order perturbation theory. Using first-principles quantum transport simulation, we validate our theory with three cases of the black phosphorus-like Bi (in-plane ferroelectric), monolayer α-GeTe (out-of-plane ferroelectric), and α-In$_2$Se$_3$ (in-plane and out-of-plane coupled ferroelectric).

This paper is organized as follows: After introducing our computation method, we first present the theoretical model of the spin photogalvanic effect and the spin orbit coupling effect in 2D ferroelectric (FE) semiconductors. Second, through symmetry analysis, we obtained the general behaviors of the spin photogalvanic effect in 2D van der Waals ferroelectric materials under ferroelectric modulation. Finally, we verified our theoretical model by performing first-principles calculations on 2D vdW FE semiconductors α-GeTe [6], BP-Bi [42], and α-In$_2$Se$_3$ [36].

TABLE I. Table of the spin photogalvanic effect under the control of ferroelectric polarization in different ferroelectric materials with the spin-orbit coupling effect. L and C denote the linearly and circularly polarized light, respectively. T and N refer to tunable and nontunable by the ferroelectric polarization switch, respectively.

Polarization	Light	e	S^x	S^y	S^z
P_{in}	L	T	N	N	T
	C	T	T	T	N
P_{OOP}	L	N	T	T	N
	C	N	T	T	N
P_{cp}	L	T	T	T	T
	C	T	T	T	T

II. COMPUTATIONAL METHOD

The first-principles calculations are based on the density-functional theory (DFT). A vacuum layer of over $15\,\text{Å}$ in the atomic and device models, the generalized gradient approximation (GGA) for the exchange-correlation functional, and the Perdew-Burke-Ernzerhof (PBE) form [43] are used for geometric optimizations. The geometric optimizations are carried out using the projector augmented-wave pseudopotentials and plane-wave basis set, as implemented in the Vienna *Ab initio* Simulation Package (VASP) package [44–46]. The force tolerance on each atom is less than $10^{-2}\,\text{eV/Å}$, and the converged energy is less than $10^{-5}\,\text{eV}$ per unit cell. The spin configuration is calculated with the VASPKIT code with the k-point grid density of $0.01\,\text{Å}^{-1}$ [47]. The calculations of the Berry phase are conducted using the VASPBERRY code [48]. In the structural optimization of the monolayer BP-Bi, a $15\,\text{Å}$ vacuum layer, a $12 \times 12 \times 1$ k-mesh, and a cutoff energy of $400\,\text{eV}$ are used. In the structural optimization of the monolayer α-GeTe, a $15\,\text{Å}$ vacuum layer, a $12 \times 12 \times 1$ k-mesh, and a cutoff energy of $400\,\text{eV}$ are used. In the structural optimization of monolayer α-In$_2$Se$_3$, a $15\,\text{Å}$ vacuum layer, a $12 \times 12 \times 1$ k-mesh, and a cutoff energy of $500\,\text{eV}$ are employed.

The transport simulation is performed with the DFT coupled with the nonequilibrium Green's function (NEGF) approach [49–52]. The transport properties are calculated with the psedoDojo-SO pseudopotential with high basis set of the linear combination of atomic orbital for the fully relativistic calculation, as implemented in the QUANTUMATK package [53]. The generalized gradient approximation with the spin orbit coupling (SOGGA) for the exchange-correlation functional, and the Perdew-Burke-Ernzerhof form with the spin orbit coupling (SOGGA. PBE) are used during the transport simulation. The k mesh grids for the electrodes and central region are set $20 \times 1 \times 139$ and $20 \times 1 \times 1$, respectively [53]. The electronic temperature of $300\,\text{K}$ is used for the transport calculation. For the transport calculations of BP-Bi, α-GeTe, and α-In$_2$Se$_3$, the broadening temperatures are set to 1000, 1000, and 500 K, respectively. The periodic, Neumann, and Dirichlet boundary conditions are set in outward direction perpendicular to the plane, vacuum layer direction, and electron transport direction, respectively.

In the transport simulation, the nonequilibrium Green's function method describes the behavior of a finite quantum open system under the influence of an equilibrium thermal reservoir (electronic or photonic) in terms of the current flow. The physical quantities of the studied system are described by the reduced density matrix obtained by taking the trace over the thermal reservoir. The Hamiltonian of the system with the dipole approximation is [52]

$$H = H_0 + \frac{e}{m_0}\mathbf{A}_\omega \cdot \mathbf{P} = H_0 + H_I, \quad (1)$$

where e is the electron charge, m_0 is the free-electron mass, $\bar{h}$ is the reduced Planck constant. H_0 is the Hamiltonian without the electron-light interaction. H_0 is the Hamiltonian considering the interaction between the central region and the electrodes, commonly used in electronic transport calculations, as shown in these works. H_I is the electron-light

interaction, $\mathbf{p}$ the momentum operator, and A_ω the electromagnetic vector potential from a single-mode monochromatic light source with frequency ω. The greater and lesser Green's functions $G^{>/<}$ of H are calculated by [54]

$$G^{>/<} = G_0^r (\Sigma_R^{>/<} + \Sigma_L^{>/<} + \Sigma_{ph}^{>/<}) G_0^a, \quad (2)$$

where $G_0^{R,>,<}$ denote the retarded noninteracting Green's functions, and $\Sigma_{L,R,ph}^{>,<}$ are the lesser and greater self-energies due to coupling to the electrodes and light, respectively. The self-energies are calculated by the first Born approximation, i.e., $\Sigma_{ph}^{>/<}G^{>/<} = H_I G_0^{><}$. The electron-photon self-energies are [49]

$$\Sigma_{ph}^> = [NH_I^+ G_0^>(\varepsilon^+)H_I + (N+1)H_I G_0^>(\varepsilon^-)H_I^+], \quad (3)$$

$$\Sigma_{ph}^< = [NH_I G_0^<(\varepsilon^-)H_I^+ + (N+1)H_I^+ G_0^<(\varepsilon^+)H_I], \quad (4)$$

where $\varepsilon_\pm = \varepsilon \pm \hbar\omega$, and N is the number of photons.

The photocurrent is in electrode α (left or right) with is calculated as [54]

$$I_\alpha = \frac{e}{\hbar} \int \frac{d\varepsilon}{2\pi} \sum_{k^\parallel} \text{Tr}[i\Gamma_\alpha(\varepsilon, k^\parallel)][1 - f_\alpha]G^< + f_\alpha G^>], \quad (5)$$

where ε *is* the energy, $k^\parallel$ is the wave vector perpendicular to the transmission direction, and $\Gamma_\alpha(\varepsilon, k^\parallel)$ is the broadening function of the interaction between the systems and the electrodes. Our calculation takes the photocurrent flowing into the left electrode, which is equivalent to the photocurrent flowing out of the right electrode, i.e., $I_L = -I_R$ [54].

When the NEGF method is coupled with DFT, the density matrix obtained through G_0 will iteratively self-consist with the density matrix obtained from the Kohn-Sham equation, ultimately yielding the converged density matrix. Subsequently, the photocurrent is obtained through the aforementioned non-self-consistent process due to the first Born approximation [52]. After considering spin space, the electron density obtained from the Kohn-Sham equation for different spin components self-consistently matches the electron density obtained from the Green's function method, yielding the corresponding spin component of the Green's function.

In the absence of the SOC, considering spin space only requires taking the direct product of the density matrix in spin space and the density matrix in coordinate space. However, when the SOC is included, the spin space and the coordinate space are entangled. The wave function is a two-component spinor [21,55]:

$$\psi_i(r) = \begin{pmatrix} \alpha_i(r) \\ \beta_i(r) \end{pmatrix}, \quad (6)$$

where α, β denotes the spin-up and down, respectively.

Here we can introduce the noncollinear density matrix in the spin space:

$$n(r) = \sum_i^{\text{occ}} \psi_i^+(r)\psi_i(r) = \begin{bmatrix} n_{\alpha\alpha} & n_{\alpha\beta} \\ n_{\beta\alpha} & n_{\beta\beta} \end{bmatrix}. \quad (7)$$

The photocurrent is expressed as

$$\langle I_{ph}^{\sigma} \rangle = \mathrm{Tr}\left[\frac{1}{2}\{ev,\sigma\}n(r)\right] = \frac{1}{2}\sum_{i}^{\mathrm{occ}}\psi_{i\alpha}^{+}(r)\{ev,\sigma\}_{\alpha\beta}\psi_{i\beta}(r),$$
(8)

where v is the velocity of the electrons, and $\boldsymbol{\sigma}$ is the Pauli matrix. For each component, we can obtain the spin-dependent density matrix in NEGF through the aforementioned DFT+NEGF coupling method, thus obtaining the self-consistent spin-dependent nonequilibrium Green's function and transport properties.

By including the unit matrix I, the photocurrent with non-collinear spin can be expressed as a 2×2 matrix, which contains the total photocurrent (charge current) and the spin photocurrent projected to each directions i:

$$I_{ph} = \begin{bmatrix} I_{sum} & I_{\sigma_x} \\ I_{\sigma_y} & I_{\sigma_z} \end{bmatrix}$$
$$= \begin{bmatrix} I_{ph}^{\mathrm{up,up}} + I_{ph}^{\mathrm{down,down}} & 2\mathrm{Re}I_{ph}^{\mathrm{up,down}} \\ -2\mathrm{Im}I_{ph}^{\mathrm{up,down}} & I_{ph}^{\mathrm{up,up}} - I_{ph}^{\mathrm{down,down}} \end{bmatrix}. \quad (9)$$

The σ_i denotes the spin projection along the i direction ($i = x$, y, and z). The magnetic quantum axis z is chosen to be vertical to the vdW planes in this work. Here, we emphasize that the spin current in this work includes an additional constant, e, compared to the general definition of spin current. However, this does not affect the main conclusions of this work.

To normalize the photocurrent with respect to the incident optical power, we define the photoresponse (R) as the ratio of the photocurrent to the incident light power [56]:

$$R = \frac{I_{\mathrm{ph}}}{P_{\mathrm{ph}}}, \quad (10)$$

$$P_{\mathrm{ph}} = SI_{\omega}E_{\mathrm{ph}}, \quad (11)$$

where P_{ph} is the incident light power. $S = 64.89$, 107.26, and 87.68 Å^2 are the illumination area of the BP-Bi, α-GeTe, and α-In$_2$Se$_3$ photodetectors in the calculation, respectively. $I_{\omega} = 1\,\text{s}^{-1}\,\text{Å}^{-2}$ is the photon flux, and E_{ph} is the photon energy. In this paper, we only consider the case of light being vertically incident on the two-dimensional plane. The two polarization vectors of the light correspond to the x and y directions in their respective figures.

III. THEORETICAL BACKGROUND

A. Spin photogalvanic effect

The SPGE refers to the effect where a system generates a spin current under a uniform illumination of light, which is a second-order response to the electric fields. The spin current is defined as the anticommutator of the velocity operator and the spin operator, i.e., $J_c^{S_i} = \frac{1}{2}\{v_c,S_i\} = \frac{1}{2}(v_cS_i + S_iv_c)$, where S_i ($i =, x, y,$ and z) denotes the S_x, S_y, and S_z, respectively. It is worth noting that when $S^i = e$, the above definition becomes the definition of charge current. By using the second-order perturbation theory, the response coefficient σ of the SPGE

can be obtained as [1]

$$\langle \sigma_{b,c}^{a,S_i} \rangle^{(2)}(\omega,-\omega) = \frac{e^2}{\omega^2} \int \frac{dk^d}{(2\pi)^d} \sum_{mnl} \frac{f_{lm}v^b{}_{lm}}{E_{mn} - \hbar\omega + \frac{i\hbar}{\tau}}$$
$$\times \left(\frac{j_{mn}^{a,S_i}v_{nl}^c}{E_{ml} + \frac{i\hbar}{\tau}} - \frac{v_{mn}^c j_{nl}^{a,S_i}}{E_{ln} + \frac{i\hbar}{\tau}} \right), \quad (12)$$

where the real and imaginary parts of σ refer to the direct-current conductivities under the linearly-polarized and circularly polarized light, respectively. By distinguishing the diagonal ($m = n$) and off-diagonal terms ($m \neq n$) of the nonequilibrium density matrix, SPGE can also be categorized into four mechanisms, similar to the photogalvanic effect [4]. These four mechanisms are linear injection spin current, linear shift spin current, circular injection spin current, and circular shift spin current, where the injection and shift terms refer to the diagonal and off-diagonal terms, respectively. We can drive the following formulas:

The linear injection spin current is

$$\eta_{abc}^{L,i}(\omega) = -\frac{\pi e^2}{2\hbar^2\omega^2}\sum_{mn}dk^3\alpha_{mn}^{ab}(k)[\{S_i,v^c(k)\}_{mm}$$
$$- \{S_i,v^c(k)\}_{nn}]\tau\delta(\omega - \omega_{mn}). \quad (13)$$

The linear shift spin current is

$$\eta_{abc}^{L,i}(\omega) = \frac{\pi e^2}{2\hbar^2\omega^3}\sum_{mn}dk^3\alpha_{mn}^{ab}(k)\{R^c(k),S_i\}_{nm}\delta(\omega - \omega_{mn}).$$
(14)

The circular injection spin current is

$$\eta_{abc}^{C,i}(\omega) = \frac{i\pi e^2}{\hbar^2\omega^2}\sum_{mn}dk^3\mathrm{Im}\left(v_{mn}^a(k)v_{nm}^b(k)\right)[\{S_i,v^c(k)\}_{mm}$$
$$- \{S_i,v^c(k)\}_{nn}]\tau\delta(\omega - \omega_{mn}). \quad (15)$$

The circular shift spin current is

$$\eta_{abc}^{L,i}(\omega) = \frac{-i\pi e^2}{\hbar^2\omega^3}\sum_{mn}dk^3\mathrm{Im}\left[v_{mn}^a(k)v_{nm}^b(k)\right]\{R^c(k),S_i\}_{nm}$$
$$\times \delta(\omega - \omega_{mn}). \quad (16)$$

Here $\alpha_{mn}^{ab}(k) = \frac{1}{2}[v_{mn}^a(k)v_{nm}^b(k) + v_{mn}^b(k)v_{nm}^a(k)]$ is the optical oscillate strength [3], and $R_{nm}^c(k) = \frac{\partial\phi_{nm}^b}{\partial k^c} + \xi_{nn}^c - \xi_{mm}^c$ is the shift vector [19]. $\Omega^c(k) = \mathrm{Im}[v_{mn}^a(k)v_{nm}^b(k)]E_{mn}^2$ is the Berry curvature [26].

B. Spin orbit coupling in 2D vdW ferroelectric

The spin orbit coupling arise from the motion of the electric field at a high speed, resulting in a magnetic field, i.e., $H_{SO} = \mathbf{B}_{eff} \cdot \boldsymbol{\sigma} = \lambda(\mathbf{v} \times \mathbf{E}) \cdot \boldsymbol{\sigma} = \lambda_R(\mathbf{k} \times \mathbf{E}) \cdot \boldsymbol{\sigma}$ [20]. In 2D vdW ferroelectric systems, there are three types of ferroelectric orders: the in-plane ferroelectricity ($\boldsymbol{P}_{in}$), the out-of-plane ferroelectricity ($\boldsymbol{P}_{oop}$), and the in-plane and out-of-plane coupled ferroelectricity ($\boldsymbol{P}_{cp}$), corresponding to the electric field of $\mathbf{E}_{in} = (E_x, E_y, 0)$, $\mathbf{E}_{oop} = (0, 0, E_z)$, and $\mathbf{E}_{cp} = (E_x, E_y, E_z)$, respectively [57]. Here, the in-plane and out-of-plane ferroelectric polarizations correspond to Ising- and Rashba-type spin splittings, respectively. The Hamiltonian of the Ising type

SOC is expressed as: $H_{Is} = (k_x E_y - E_x k_y)\sigma_z$, and that of the Rashba type SOC is $H_{Ra} = E_z(k_y\sigma_x - k_x\sigma_y)$ [41,58].

The Ising-type spin splitting causes band splitting in the S_z direction (vertical to the vdW plane), similar to the 2D Ising model. This phenomenon corresponds to the spin-momentum locking effect in valleytronics materials such as MoS_2 and $MoSi_2N_4$ [27,59]. On the contrary, the Rashba-type spin-splitting causes chiral splitting in the S_x and S_y components within the vdW plane [41]. In applications, the Rashba effect is often used for the spin-orbit torque, which involves injecting a current into a heavy metal to generate a spin current and twist the magnetic moment of a magnetic tunnel junction [60]. In theory, the Rashba effect has also been proposed as a principle for the Datta-Dias spin transistors [29].

In practical band structure calculations, the SOC effects are incorporated through perturbation terms. The Rashba and Ising spin splittings mentioned earlier correspond to first-order perturbations, while the Dresselhaus effect arises when considering the higher-order perturbations [61]. Due to the complexity of higher-order perturbations, the Dresselhaus effect cannot be expressed in a general formula. We can only infer that due to the breaking of spatial inversion symmetry, higher-order perturbations must be odd powers of k. For example, the 3D Dresselhaus Hamiltonian with bulk inversion asymmetry is expressed as $\gamma[k_x(k_y^2 - k_z^2)\sigma_x + k_y(k_z^2 - k_x^2)\sigma_y + k_z(k_x^2 - k_y^2)\sigma_z]$, where γ is a material constant. On account of the confined electrons along z direction, 3D Dresselhaus Hamiltonian can be transformed to the 2D counterpart, i.e., $\beta(k_x\sigma_x - k_y\sigma_y)$ [41].

In the model presented in this paper, we neglect the Dresselhaus effect for two reasons. Firstly, as a higher-order perturbation, the Dresselhaus effect is weaker than the first-order perturbation of intensity, and there are currently no examples where the Dresselhaus effect can exist independently of the Rashba effect. Secondly, the Dresselhaus effect has various forms of Hamiltonians according to different symmetries, which makes it difficult to analyze and impossible to give a widely applicable form. When encountering the occurrence of Dresselhaus effect in materials, a specific analysis needs to be conducted based on the specific spin splitting types, followed by symmetry analysis [61].

IV. TUNABLE SPGE IN 2D VDW FERROELECTRICS WITH SPIN ORBIT COUPLING

A. Theoretical model

We transform the problem of analyzing the symmetry of SPGE coefficients into an analysis of the symmetry of the four physical quantities that constitute them. These four physical quantities are the matrix elements of the optical harmonic intensity $\alpha_{mn}(k)$, Berry curvature $\Omega_n(k)$, group velocity of electronic wave packets $v_{nn}(k)$, and displacement difference of electronic wave packets before and after excitation $R_{mn}(k)$. In time-reversal invariant systems, $v_{nn}(k)$ and $\Omega_n(k)$ are odd under the spatial inversion, while $\alpha_{mn}(k)$ and $R_{mn}(k)$ are even under the spatial inversion. Based on this symmetry relationship, it can be derived that linear injection current and circular shift current only contribute to spin currents in SPGE, while linear shift current and circular injection current only

contribute to charge currents, which is firstly proposed by Fei *et al.* [3]. Besides, as the strength of SOC weakens, the spin photocurrent vanishes to zero [1].

Next, we consider the symmetry properties of $\alpha_{mn}(k)$, $\Omega_n(k)$, $\{R(k), S_i\}_{mn}$, and $\{v(k), S^i\}_{nn}$, under ferroelectric polarization reversal. For convenience of description without loss of generality, we define a certain state before the reversal as $\varphi_1(k)$, and a state after the reversal as $\varphi_2(k)$. It should be noted that $\varphi_2(k)$ is not the quantum state obtained by performing ferroelectric inversion on $\varphi_1(k)$, but rather a new quantum state with the same wave function k in the same coordinate system after the reversal. Since the k-space coordinate system remains unchanged after the ferroelectric reversal, measuring the wave vectors of $\varphi_1(k)$ and $\varphi_2(k)$ both yield k. However, the spin and phase information of the original $-k$ wave function are preserved, resulting in the Berry curvature, Berry connection, and spin eigenvalues as those of $\varphi_1(-k)$.

In the Ising-type vdW ferroelectrics (assuming the crystal structure perpendicular to the ferroelectric direction is symmetric), the photocurrent transport direction and the ferroelectric polarization are set both along the same direction. For simplicity, we assume that the in-plane polarized ferroelectric materials possess mirror inversion symmetry along the direction perpendicular to the plane, which is also common in 2D in-plane ferroelectric materials such as BP-Bi and MX (M = Ge, Sn; X = S, Se) [42,62]. Therefore, the in-plane ferroelectric reversal (mirror reflection operation) can be regarded as the spatial reversal operation at the gamma point, which is also very common in ferroelectric materials. The eigenvalues of S_z, $\{S_i, R_{nm}(k)\}$, and $\Omega_n(k)$ will change to $-S_z$, $\{S_i, R_{nm}(k)\}$, and $-\Omega_n(k)$, respectively.

In the Rashba-type ferroelectrics, the symmetry change caused by the out-of-plane ferroelectric polarization reversal ($\boldsymbol{P}_{oop}$) is completely different. This is because the ferroelectric polarization is along the direction perpendicular to the vdW plane, so the velocity and phase of the wave function are not changed. Only the eigenvalues of the spin in the 2D plane undergo changes. This is the main distinction between the out-of-plane and in-plane ferroelectric polarization in modulating the SPGE. In 2D ferroelectric systems, the Berry curvature and Berry connection change sign under the reversal of $\boldsymbol{P}_{in}$, while they remain unchanged under the reversal of $\boldsymbol{P}_{oop}$. For in-plane and out-of-plane coupled ferroelectric materials, we only need to combine the above two cases. In the following, we will discuss the forms of the SPGE under linearly polarized and circularly polarized light in different types of vdW ferroelectric materials.

B. In-plane ferroelectric

For the sake of convenience, we define $|\uparrow_i\rangle$ and $|\downarrow_i\rangle$ (i = x, y, and z) as the different spin eigenstates of S_i, and define $|k, \uparrow_i/\downarrow_i\rangle$ as the eigenstate of the total Hamiltonian throughout this paper. We first focus on Ising-type SOC ferroelectric materials, which correspond to materials such as SnS, SnSe [62], SnTe [63], and black phosphoruslike Bi (BP-Bi) [42,64]. The spin is split along the S_z direction, allowing for spin current contribution in the S_z direction, while the S_x and S_y contribute only to the charge current, i.e., $\langle\uparrow_z|S_{x,y}|\uparrow_z\rangle = \langle\downarrow_z|S_{x,y}|\downarrow_z\rangle = 0$ and $\langle\downarrow_z|S_{x,y}|\uparrow_z\rangle =$

$\langle\uparrow_z|S_{x,y}|\downarrow_z\rangle = \frac{\hbar}{2}$. In systems with time-reversal symmetry, the spin current is contributed by the linearly injection current and circularly shift current, and is solely in the S_z component. In contrast, the charge current is contributed by the linear shift current and circular injection current, and is generated from the S_x and S_y of the SPGE coefficients (of course, there is also the role of the identity matrix I, which corresponds to the photogalvanic effect, but this is not the main focus of this article). The mechanism of SPGE in the in-plane ferroelectrics (Ising-type spin split) is summarized as follows:

The linear injection current contributes to a tunable spin current:

$$\alpha\{v, S_z\}(k, \uparrow_z) \overset{P}{\to} \alpha(k)\{v(k), S_z\}(k, \downarrow_z). \tag{17}$$

The linear shift current contributes to a nontunable charge current:

$$\alpha\{R, S_{x,y}\}(k, \uparrow_z) \overset{P}{\to} \alpha\{R, S_{x,y}\}(k, \downarrow_z) = \alpha\{R, S_{x,y}\}(k, \uparrow_z). \tag{18}$$

The circular injection contributes to a tunable charge current:

$$\Omega\{v, S_{x,y}\}(k, \uparrow_z) \overset{P}{\to} -\Omega\{v, S_{x,y}\}(k, \downarrow_z) = -\Omega\{v, S_{x,y}\}(k, \uparrow_z). \tag{19}$$

The circular shift current contributes to a nontunable spin current:

$$\Omega\{R, S_z\}(k, \uparrow_z) \overset{P}{\to} -\Omega\{R, S_z\}(k, \downarrow_z) = \Omega\{R, S_z\}(k, \uparrow_z). \tag{20}$$

Here, we only discuss the case where the ferroelectric polarization direction is parallel to the photocurrent transport direction, as this is the most relevant aspect of the PGE [65]. If we replace S_i with e, the charge current of the PGE is obtained. It can be easily proved that the charge current of PGE changes its sign under the Ising-type ferroelectric reversal, which is accordance with the previous reports [4,66].

Here is another interesting point: Typically, we tend to assume that ferroelectric polarization reversal accompanied by SOC would always control the corresponding split component of the spin current. For example, Fei et al. previously calculated the SPGE in the Rashba and Dresselhaus semiconductor (bulk α-GeTe) under the linearly injection current [6]. However, under the circularly polarized light, the S_z spin currents generated in the Ising-type ferroelectrics is not controlled by the ferroelectric polarization reversal. This phenomenon is intriguing because it is counterintuitive; the current along the transport direction is not influenced by the ferroelectricity along the same direction, which is also opposite to the PGE. The reason for this contradiction lies in the time-reversal symmetry of spin currents, which means that a spin current flowing upwards and to the left is equivalent to a spin current flowing downwards and to the right. The ferroelectric modulation simultaneously changes the directions of both spin and transport, resulting in an apparent preservation of the spin current. We refer to this effect as the hidden spin current modulation.

C. Out-of-plane ferroelectric

Similarly, we can derive the form of SPGE in the out-of-plane ferroelectrics (Rashba-type spin split) that is modulated by ferroelectric polarization. In practice, this corresponds to materials such as $AgBiP_2Se_6$ [67], distort 1T-$MoTe_2$ [68], $CuInP_2S_6$ [69], $CuInP_2Se_6$ [70], α-GeTe [71], sliding h-BN [72,73], and sliding WTe_2 [74].

In the out-of-plane ferroelectric, the linear injection current contributes to a tunable spin current:

$$\alpha\{v, S_{x,y}\}(k, \uparrow_{x,y}) \overset{P}{\to} \alpha\{v, S_{x,y}\}(k, \downarrow_{x,y}). \tag{21}$$

The linear shift current contributes to a nontunable charge current:

$$\alpha\{R, S_z\}(k, \uparrow_{x,y}) \overset{P}{\to} \alpha\{R, S_z\}(k, \downarrow_{x,y}) = \alpha\{R, S_z\}(k, \uparrow_{x,y}). \tag{22}$$

The circular injection contributes to a nontunable charge current:

$$\Omega\{v, S_z\}(k, \uparrow_{x,y}) \overset{P}{\to} \Omega\{v, S_z\}(k, \downarrow_{x,y}) = \Omega\{v, S_z\}(k, \uparrow_{x,y}). \tag{23}$$

The circular shift current contributes to a tunable spin current:

$$\Omega\{R, S_{x,y}\}(k, \uparrow_{x,y}) \overset{P}{\to} \Omega\{R, S_{x,y}\}(k, \downarrow_{x,y}). \tag{24}$$

We can see that the ferroelectric modulation of the SPGE in both Rashba and Ising types is consistent under the linearly polarized light, but is exactly opposite under the circularly polarized light. Under the circularly polarized light, the ferroelectric modulation of SPGE in Rashba type is exactly opposite to that in Ising type: the spin current can be controlled by out-of-plane ferroelectricity, while the charge current cannot. This is because circularly polarized light is directly related to the Berry curvature. In a system with the time-reversal symmetry and the broken of the spatial inversion symmetry, the Berry curvature in wave-vector space is nonzero and odd-symmetric, i.e., $\Omega(k) = -\Omega(-k)$. The Berry curvature changes sign under in-plane ferroelectric polarization reversal, but does not change under out-of-plane ferroelectric polarization reversal. This leads to a distinct difference in the SPGE effects between in-plane and out-of-plane ferroelectric materials under circularly polarized light. On the contrary, the physical quantity corresponding to the SPGE excited by linearly polarized light is the optical resonance intensity, which is an even function in k space, i.e., $\alpha(k) = \alpha(-k)$. Therefore, the behaviors of the Ising and Rashba-type ferroelectrics under linear polarization are consistent, as both can have the direction of the spin current components split by ferroelectric modulation.

D. In-plane and out-of-plane coupled ferroelectric

The in-plane and out-of-plane coupled vdW ferroelectrics (P_{cp}) refers to materials that exhibit both in-plane and out-of-plane ferroelectric polarizations, and changing the polarization in one direction can simultaneously control the polarization in the other direction. Currently, there are not many materials that exhibit this type of coupled ferroelectric

behavior experimentally, with α-In$_2$Se$_3$ being a commonly observed material with such properties [75]. However, theoretically, there are many more materials in this category. For example, Ji *et al.* identified 61 out of the total 80 layer groups for bilayer sliding ferroelectric systems that allow for the existence of the coupled ferroelectricity [57]. Due to spin splitting in the S_x, S_y, and S_z directions, the coupled ferroelectrics exhibit spin-polarized current through all the mechanisms of SPGE. The specific forms are as follows:

The linear injection current contributes to a tunable spin current:

$$\alpha\{v, S_{x,y,z}\}(k, \uparrow_{x,y,z}) \xrightarrow{P} \alpha\{v, S_{x,y,z}\}(k, \downarrow_{x,y,z}). \quad (25)$$

The linear shift current contributes to a tunable charge current:

$$\alpha\{R, I\}(k, \uparrow_{x,y,z}) \xrightarrow{P} -\alpha\{R, I\}(k, \downarrow_{x,y,z}) = -\alpha\{R, I\}(k, \uparrow_{x,y,z}). \quad (26)$$

The circular injection contributes to a tunable charge current:

$$\Omega\{v, I\}(k, \uparrow_{x,y,z}) \xrightarrow{P} -\Omega\{v, I\}(k, \downarrow_{x,y,z})$$
$$= -\Omega\{v, I\}(k, \uparrow_{x,y,z}). \quad (27)$$

The circular shift current contributes to a tunable spin current:

$$\Omega\{R, S_{x,y,z}\}(k, \uparrow_{x,y,z}) \xrightarrow{P} -\Omega\{R, S_{x,y,z}\}(k, \downarrow_{x,y,z}). \quad (28)$$

For coupled ferroelectrics, the manipulation of the ferroelectric polarization orientation yields controllable spin currents in response to both linearly and circularly polarized light, with the tunability across all three spin projection directions. Due to the time-reversal symmetry of the system, the charge current can only be provided by the photogalvanic effect. To summarize, we have compiled the manifestations of the charge current and spin current under the control of ferroelectric polarization in different ferroelectric systems in Table I.

V. FIRST-PRINCIPLES QUANTUM TRANSPORT SIMULATION

In this section, we employ first-principles calculations coupled with NEGF method to validate our theory in several van der Waals ferroelectric materials. Here we need to clarify two things: (1) When using the NEGF method, it is impossible to distinguish between the diagonal elements (injection current) and the off-diagonal elements (shift current) of the nonequilibrium density matrix [4,18]. Therefore, the "spin current" obtained in our calculations contains both the injection current and shift current components. However, due to the time-reversal symmetry of the system, the spin current only includes linear injection current and circular shift current, while the charge current only contains the linear shift current and circular injection current. (2) In high-order perturbation theory, the relaxation time approximation is introduced, leading to the appearance of the relaxation time term in the calculation results. The value of the relaxation time is mostly given by experimental values and estimates [7], or
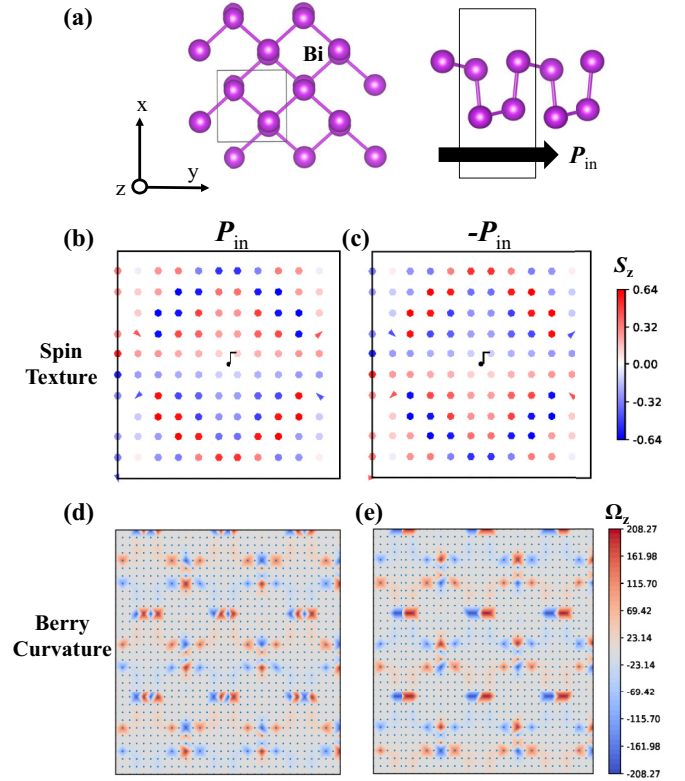

FIG. 2. (a) Geometry of the black phosphoruslike monolayer Bi (BP-Bi). Spin texture (b) and (c) and Berry curvature (d) and (e) of the valence band of BP-Bi under the ferroelectric polarizations of $\boldsymbol{P}_{\text{in}}$ and $-\boldsymbol{P}_{\text{in}}$, respectively.

directly calculated by considering phonon scattering effects [76]. In the NEGF method, the photocurrent is described by nonequilibrium Green's functions that take into account the photoelectric interaction. Taking the general Green's function as an example, if we perform a Fourier transform with respect to energy-time, it can be viewed as a quasiparticle. The imaginary part of the quasiparticle is determined by the self-energy term of the Green's function, representing its lifetime. In the calculations presented in the main text, all our circularly polarized light is right-handed. Data for the spin currents induced by left-handed circularly polarized light are provided in the Supplemental Material [77,78], and they exhibit similar properties under ferroelectric modulation as those induced by right-handed circularly polarized light.

A. Black phosphorus-like Bi (BP-Bi): Ising-type

BP-Bi is a 2D vdW ferroelectric semiconductor with the experimental bandgap of 0.27 eV [42,64]. The atomic structure of BP-Bi is very similar to that of the black phosphorus, but BP-Bi possesses a buckling with a polar space group of $Pmn2_1$, as shown in Fig. 2(a). The relaxed lattice parameter are 4.78 and 4.57 Å, respectively. The thickness of the monolayer BP-Bi is 3.52 Å. The monolayer BP-Bi possesses a calculated in-plane ferroelectric polarization of 44 pC/m, which is also confirmed by the recent experiment [42,64]. Due to the pronounced relativistic effects of bismuth and the ferroelectricity exhibited by BP-Bi, we selected BP-Bi as an
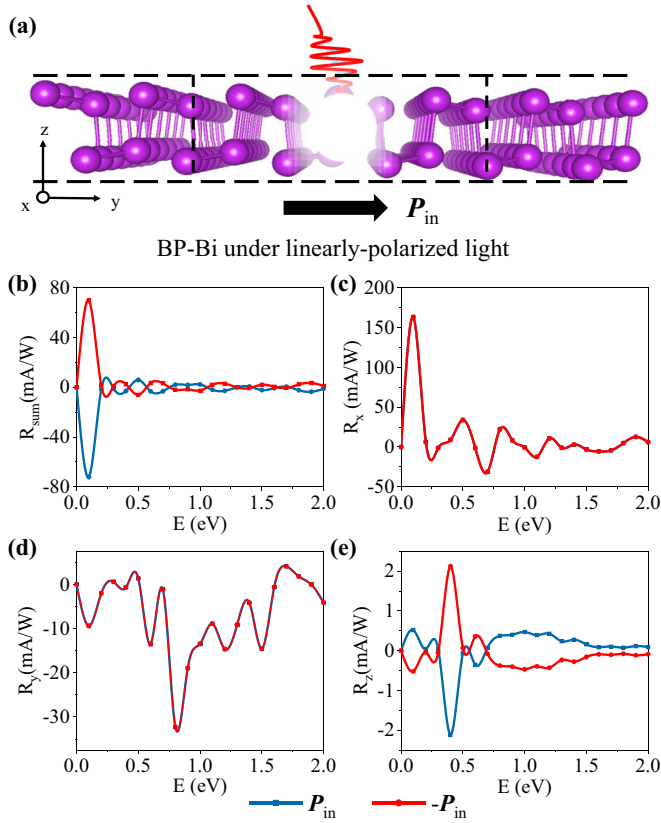
FIG. 3. (a) Schematic diagram of the BP-Bi ferroelectric photodetector with P_{in} polarization. Photoresponse of the (b) charge and spin currents (c) S_x, (d) S_y, and (e) S_z in BP-Bi under different ferroelectric polarization states of P_{in} and $-P_{in}$ upon the illumination of the y linearly polarized light.

FIG. 4. Photoresponse of the (a) charge and spin currents (b) S_x, (c) S_y, and (d) S_z in BP-Bi under different ferroelectric polarization states of P_{in} and $-P_{in}$ upon the illumination of the right-handed z circularly polarized light.

example for our study on in-plane ferroelectric polarization control of SPGE.

When considering spin-orbit coupling, the spin configuration of the valence band of BP-Bi under different ferroelectric polarizations is shown in the Figs. 2(b) and 2(c). A typical Ising-type spin splitting occurs in BP-Bi, with the spin mainly splitting in the S_z direction in the k point and the opposite spin splitting occurring at the time-reversal partner k point. Under ferroelectric polarization reversal, the direction of S_z also undergoes a corresponding reversal for certain k points. We also computed the Berry curvature of the valence band under different ferroelectric polarizations, as shown in Figs. 2(d) and 2(e). The results demonstrate that the change in in-plane ferroelectric polarization indeed leads to a sign reversal of the Berry curvature. The aforementioned variations in spin configuration and Berry curvature align well with our model.

The noncollinear spin currents of BP-Bi under different ferroelectric polarizations are shown in the Figs. 3 (linear polarized light) and 4 (circular polarized light), where the x and y components correspond to linearly polarized and circularly polarized light, respectively. As shown in Figs. 3(a) and 4(a), the charge current is reversed under the reversal of P_{in} regardless of the linearly-polarized and circularly polarized lights. The reason is that the charge current is only provided by the linear shift current and circular injection
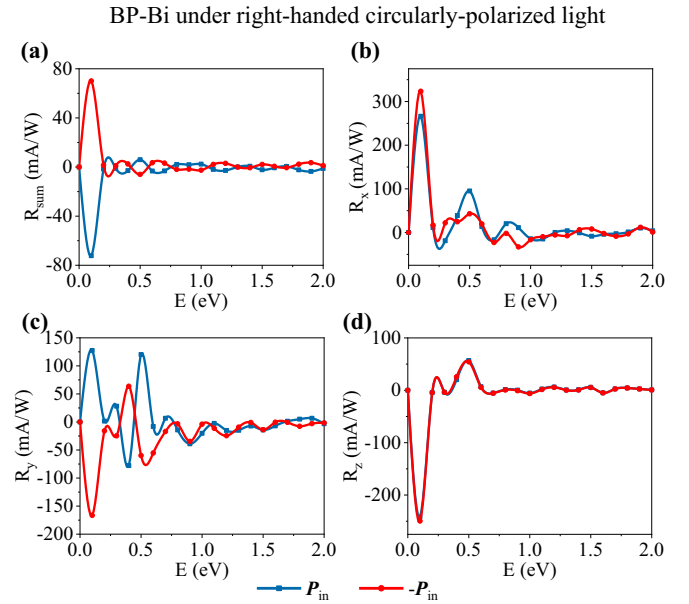
current in the T-symmetric systems. The symmetry of these two currents is determined by the Berry connection and the Berry curvature, respectively, both of which reverse under the reversal of P_{in}. Under linearly polarized light, it is observed that the spin current along the S_z component maintains an inversely proportional relationship in magnitude under different ferroelectric polarizations. However, the values of the spin currents along the S_x and S_y components remain unaffected by ferroelectric reversal. In contrast, under circularly polarized light, both the charge current and the spin currents along the S_x and S_y components can be modulated by ferroelectric polarization, while the magnitude of the spin current along the S_z component remains unaltered by ferroelectric polarization, corresponding to the hidden spin current modulation as defined in our model. We notice that under circularly polarized light, the S_x and S_y components of BP-Bi are not perfectly symmetric. We attribute this to the presence of some unknown factors in BP-Bi causing the spin to split not only along the S_z direction. As shown in Figs. 2(b) and 2(c), and Fig. S3 [77], the spin textures in the first and second valence bands actually exhibit an in-plane spin vortex that is unaffected by ferroelectric polarization, leading to the asymmetry in the S_x and S_y components of the spin photocurrents.

B. α-GeTe: Rashba-type

Monolayer α-GeTe is an out-of-plane ferroelectric semiconductor with the space group of $R3m$ and bandgap of 0.68 eV [6]. The relaxed lattice parameters of the monolayer α-GeTe is $\boldsymbol{a} = \boldsymbol{b} = 3.93$ Å, as shown in Fig. 5(a). The thickness of the monolayer α-GeTe is 1.58 Å. α-GeTe exhibits a large Rashba coefficient and a pronounced charge-to-spin conversion effect [79]. For example, α-GeTe has been successfully integrated with Si wafers, which provides a basis for the future
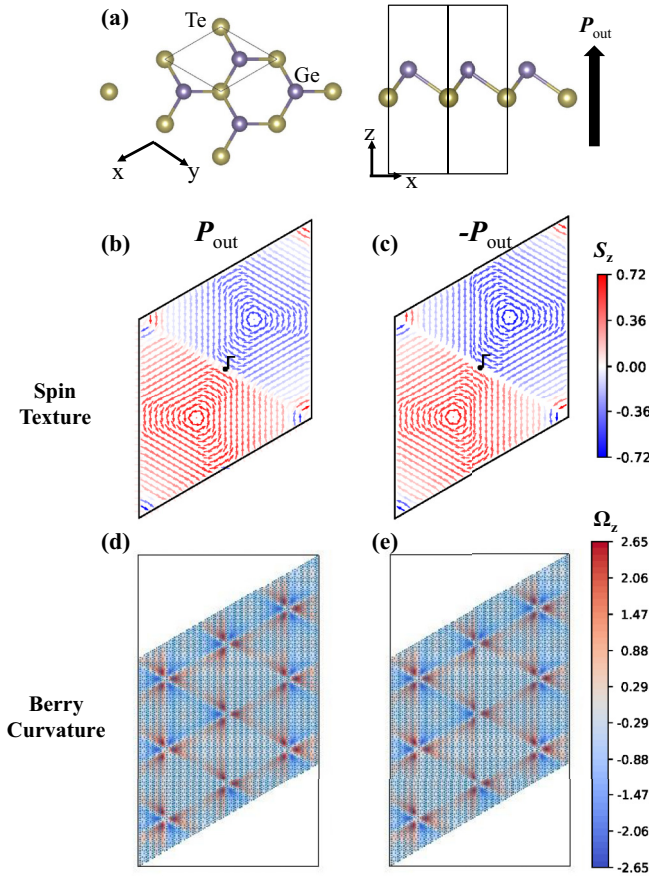
FIG. 5. (a) Schematic diagram of the monolayer α-GeTe. Spin texture (b) and (c) and Berry curvature (d) and (e) of the valence band of α-GeTe under ferroelectric polarizations of $\boldsymbol{P}_{\text{out}}$ and $-\boldsymbol{P}_{\text{out}}$, respectively.

advancement of reconfigurable, spin-based, and in-memory computing devices [71,79]. Here, we choose the monolayer α-GeTe as an example to study the out-of-plane ferroelectric control of SPGE.

In different ferroelectric polarization configurations, the Berry curvature and spin textures of the single-layer α-GeTe valence band are shown in Figs. 5(b)–5(e). It can be seen that, due to the in-plane ferroelectric polarization, the Berry curvature remains unchanged. From the spin configuration perspective, the energy bands experience splitting in the S_x, S_y, and S_z directions. The S_x and S_y configurations exhibit a helical Rashba spin splitting, and the handedness of this spin texture also changes correspondingly with the ferroelectric polarization reversal. As for the S_z component, it originates from the cubic Dresselhaus effect caused by the C_3 symmetry in GeTe, i.e., $H_{\text{SOC}} = \hbar\lambda_R(\vec{z} \times \vec{k}) \cdot \vec{\sigma} + \lambda_{cd}(k_+^3 + k_-^3)\sigma_z$ and $k_\pm = k_x \pm ik_y$ [6]. At the valence band, we did not observe a reversal of S_z due to ferroelectric polarization. However, when examining the second conduction band, it is found that the ferroelectric polarization also modulates the S_z component due to the cubic Dresselhaus effect, which would have some impact on our theoretical model that only includes the Rashba effect.

The charge current and spin current in single-layer α-GeTe under different ferroelectric polarizations are illustrated in
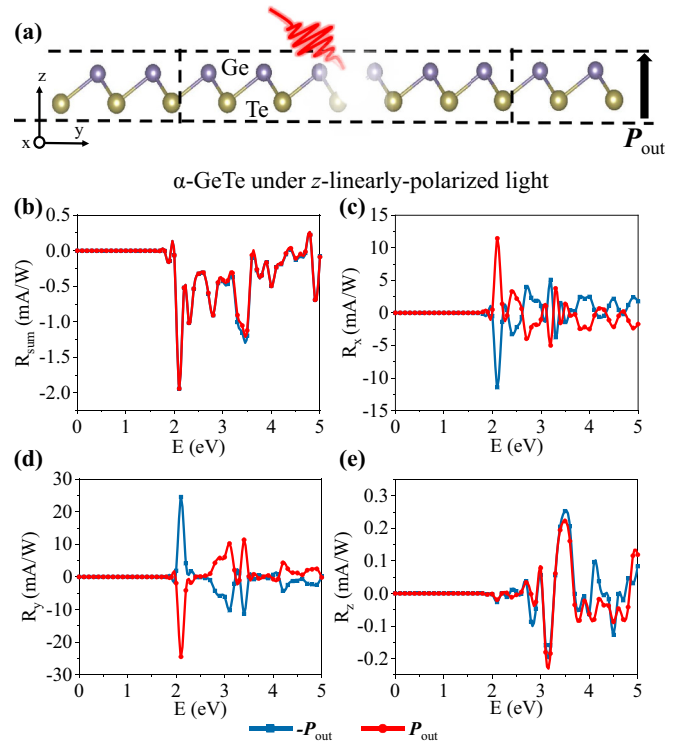

FIG. 6. (a) Geometry of the α-GeTe ferroelectric photodetector with $\boldsymbol{P}_{\text{out}}$ polarization. Photoresponse of the (b) charge and spin currents (c) S_x, (d) S_y, and (e) S_z in α-GeTe under different ferroelectric polarization states of $\boldsymbol{P}_{\text{out}}$ and $-\boldsymbol{P}_{\text{out}}$ upon the illumination of the y linearly polarized light.

the Fig. 6 (linear polarized light) and 7 (circular polarized light). As shown in Figs. 6(a) and 7(a), the charge current is unchanged under the reversal of $\boldsymbol{P}_{\text{out}}$ regardless of the linearly-polarized and circularly polarized lights. The reason is the Berry connection and the Berry curvature are unchanged under the reversal of $\boldsymbol{P}_{\text{out}}$. It can be observed that, regardless of linear or circular polarization of incident light, the S_x and S_y components undergo symmetrical changes in the direction of optoelectronic current, which arise from the Rashba-type spin splitting. On the other hand, the S_z component exhibits asymmetrical changes corresponding to the cubic Dresselhaus effect. This effect leads to a change in the spin current of the S_z component with the variation of ferroelectric polarization. The above results demonstrate that although our model performs well without considering the cubic Dresselhaus effect, it may still require modifications in certain specific material systems.

C. α-In$_2$Se$_3$: Ising+Rashba-type

α-In$_2$Se$_3$ is a unique 2D vdW semiconductor that exhibits both in-plane and out-of-plane ferroelectricity coupling, as shown in Fig. 8(a). Its monolayer has a bandgap of 1.45 eV, and the atomic structures of ML α-In$_2$Se$_3$ are arranged in a close-packed triangular lattice with an in-plane lattice constant of $\boldsymbol{a} = \boldsymbol{b} = 4.07$ Å. The thickness of the monolayer α-In$_2$Se$_3$ is 6.82 Å. In experimental studies, α-In$_2$Se$_3$ has been extensively fabricated into various ferroelectric devices with novel properties, such as ferroelectric semiconductor

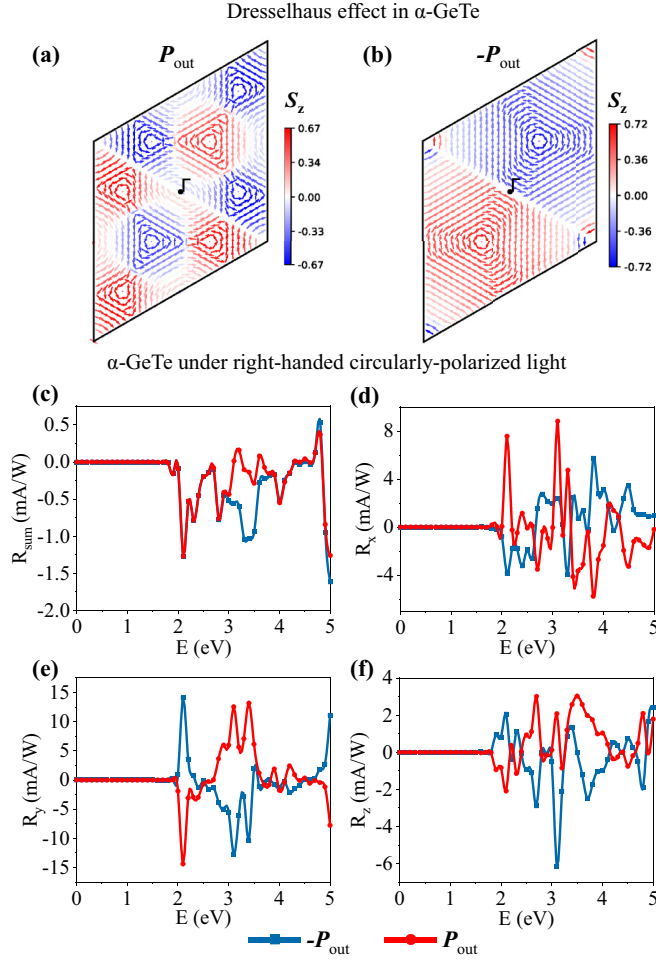FIG. 7. Spin texture of the second conduction band in the monolayer α-GeTe with the ferroelectric polarization of (a) $\boldsymbol{P}_{\text{out}}$ and (b) $-\boldsymbol{P}_{\text{out}}$. Photoresponse of the (c) charge and spin currents (d), S_x, (e) S_y, and (f), S_z in α-GeTe under different ferroelectric polarization states of $\boldsymbol{P}_{\text{out}}$ and $-\boldsymbol{P}_{\text{out}}$ upon the illumination of the right-handed z circularly polarized light.

FIG. 8. (a) Geometry of the monolayer α-In$_2$Se$_3$. Spin texture (b) and (c) and Berry curvature (d) and (e) of the valence band of α-In$_2$Se$_3$ under ferroelectric polarizations of $\boldsymbol{P}_{\text{cp}}$ and $-\boldsymbol{P}_{\text{cp}}$, respectively.

transistors [80], nonvolatile artificial neurons [81], and bidirectional optoelectronic synaptic devices [38]. On the fabrication front, α-In$_2$Se$_3$ nanosheets can now be prepared on a scale of centimeters [82]. Due to the relatively large atomic numbers of In and Se, α-In$_2$Se$_3$ also exhibits certain relativistic effects. Here, we utilize α-In$_2$Se$_3$ as an example to investigate the spin photocurrent generation efficiency in $\boldsymbol{P}_{\text{cp}}$-type ferroelectrics.

The spin configurations and Berry curvature of the valence band in α-In$_2$Se$_3$ under different polarization states are shown in the Figs. 8(b)–8(e). It can be observed that due to the presence of both in-plane and out-of-plane ferroelectricity, α-In$_2$Se$_3$ exhibits spin splitting of both Ising and Rashba types. Specifically, at the k-point corresponding to the inversion symmetric reciprocal lattice vector, S_x, S_y, and S_z are all opposite in direction, and S_x and S_y exhibit overall helical chirality. Under the reversal of ferroelectric polarization, all spin components undergo a change in direction. Additionally, due to the inversion of in-plane ferroelectric polarization, the Berry curvature of the valence band in α-In$_2$Se$_3$
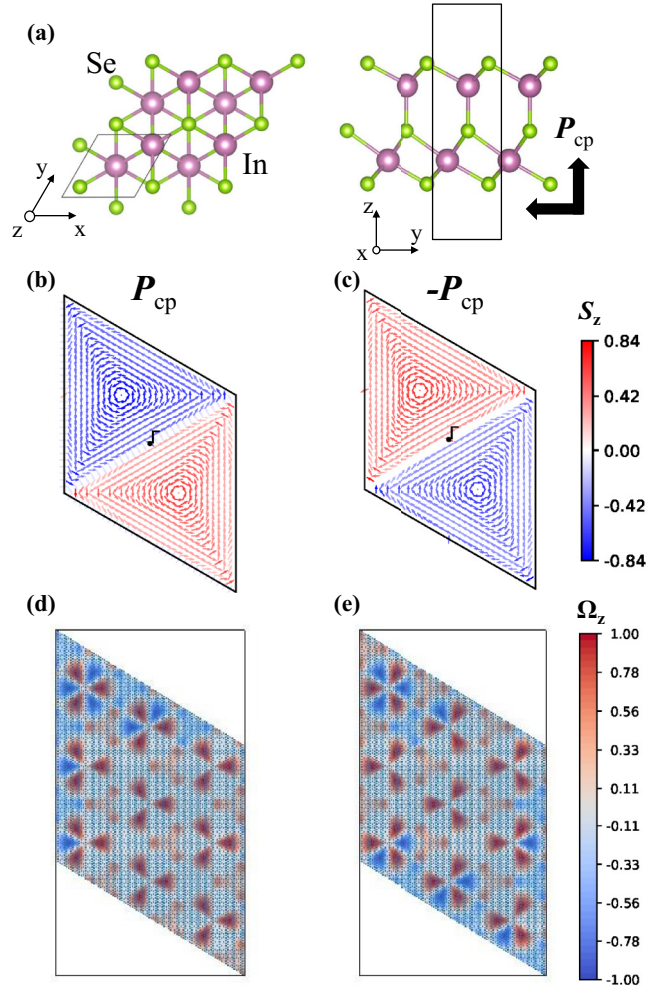
also reverses, which is similar to the calculations performed for BP-Bi.

The photoexcited noncollinear spin currents in α-In$_2$Se$_3$ under different ferroelectric polarizations are shown in Figs. 9 (linear polarized light) and 10 (circular polarized light). It can be observed that regardless of circularly or linearly polarized light, the spin currents of S_x, S_y, and S_z components undergo a change in sign upon ferroelectric polarization reversal, which is consistent with our theoretical predictions. As for the charge current [Figs. 9(b) and 10(a)], the ferroelectric reversal does not result in a sign change of charge current, which in contradiction with the general case of the PGE (photogalvanic effect). The reason for this phenomenon lies in the fact that in our DFT+NEGF calculations, the electrodes used are intrinsic α-In$_2$Se$_3$, which is a large bandgap semiconductor. This leads to very small (close to zero) generated photocurrents. To address this issue, we are only able to resort to doping the α-In$_2$Se$_3$ electrode and extending the channel to ensure that the central region is not metallized. Since our calculations have considered the SOC effect, increasing the channel length has exceeded our current computational capabilities, and thus
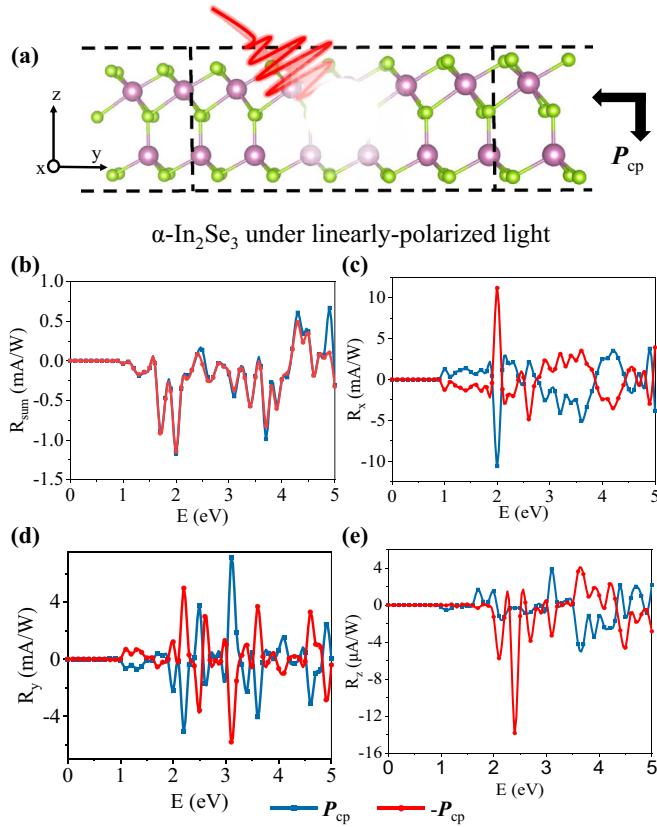
FIG. 9. (a) Schematic diagram of the α-In$_2$Se$_3$ ferroelectric photodetector with the polarization of $\boldsymbol{P}_{cp}$. Photoresponse of the (b) charge and spin currents (c) S_x, (d) S_y, and (e) S_z in α-In$_2$Se$_3$ under different ferroelectric polarization states of $\boldsymbol{P}_{cp}$ and $-\boldsymbol{P}_{cp}$ upon the illumination of the y linearly polarized light.

we do not currently have the ability to characterize this effect. However, previous works have demonstrated that in the case of electrodes doped with metals (such as the α-In$_2$Se$_3$ p-n junctions with the doped α-In$_2$Se$_3$), the photocurrent can be effectively tuned by the polarization in the case without considering the SOC [36,38].

VI. CONCLUSION

In this work, we systematically present a model for the SPGE (spin photogalvanic effect) in SOC (spin-orbit coupling) ferroelectric semiconductors under the first-order relativistic perturbation (Rashba effect), including in-plane, out-of-plane, and in-plane-out-of-plane coupled SOC. We find that in the in-plane ferroelectrics, the spin current of the S_z component can be modulated by adjusting the ferroelectricity under the linearly polarized light, but not under the circularly polarized light. In the out-of-plane ferroelectrics, both linearly
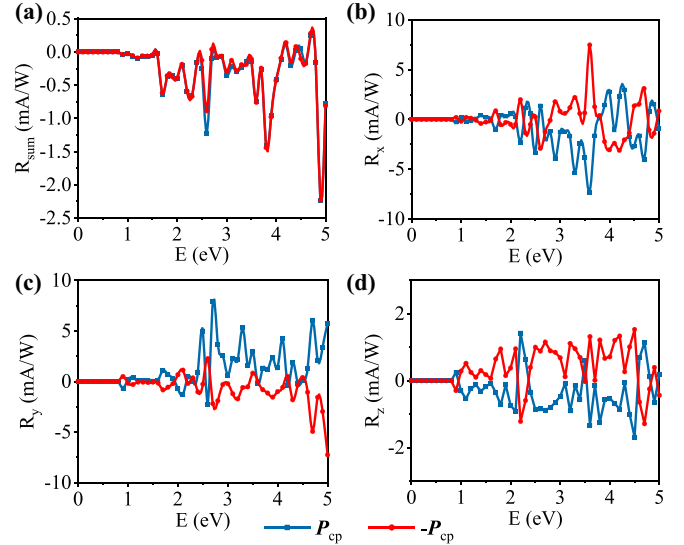

FIG. 10. Photoresponse of the (a) charge and spin currents (b) S_x, (c) S_y, and (d) S_z in α-In$_2$Se$_3$ under different ferroelectric polarization states of $\boldsymbol{P}_{cp}$ and $-\boldsymbol{P}_{cp}$ upon the illumination of the right-handed z circularly polarized light.

and circularly polarized light can modulate the spin currents of the S_x and S_y components by adjusting the ferroelectricity. In the coupled ferroelectric materials, all three spin components of the spin current can be effectively controlled by the ferroelectricity, regardless of the type of incident light. By employing first-principles calculations combined with quantum transport, we verify our model using three examples: BP-Bi, α-GeTe, and α-In$_2$Se$_3$. The results demonstrate that our model holds true when neglecting higher-order relativistic perturbations. However, when the ferroelectrics exhibit perturbations from higher-order relativistic effects (the Dresselhaus effect), specific modifications to the model are required. Our work paves the way for future research on electric-optical-magnetic coupled novel memories.

[1] H. Xu, H. Wang, J. Zhou, and J. Li, Pure spin photocurrent in noncentrosymmetric crystals: Bulk spin photovoltaic effect, Nat. Commun. **12**, 4330 (2021).

[2] S. M. Young, F. Zheng, and A. M. Rappe, Prediction of a linear spin bulk photovoltaic effect in antiferromagnets, Phys. Rev. Lett. **110**, 057201 (2013).

[3] R. Fei, X. Lu, and L. Yang, Intrinsic spin photogalvanic effect in nonmagnetic insulator, arXiv:2006.10690.

[4] Z. Dai and A. M. Rappe, Recent progress in the theory of bulk photovoltaic effect, Chem. Phys. Rev. **4**, 011303 (2023).

[5] J.-M. Lihm and C.-H. Park, Comprehensive theory of second-order spin photocurrents, Phys. Rev. B **105**, 045201 (2022).

[6] R. Fei, S. Yu, Y. Lu, L. Zhu, and L. Yang, Switchable enhanced spin photocurrent in Rashba and cubic Dresselhaus ferroelectric semiconductors, Nano Lett. **21**, 2265 (2021).

[7] R. Fei, W. Song, L. Pusey-Nazzaro, and L. Yang, *PT*-Symmetry-Enabled spin circular photogalvanic effect in antiferromagnetic insulators, Phys. Rev. Lett. **127**, 207402 (2021).

[8] X. Jiang, L. Ye, X. Wu, L. Kang, and B. Huang, Role of large Rashba spin-orbit coupling in second-order nonlinear optical effects of polar BiB_3O_6, Phys. Rev. B **106**, 195126 (2022).

[9] M. V. Entin and V. M. Kovalev, Nonlinear circular valley photogalvanic effect, Phys. Rev. B **104**, 075424 (2021).

[10] X. Mu, Q. Xue, Y. Sun, and J. Zhou, Magnetic proximity enabled bulk photovoltaic effects in van der Waals heterostructures, Phys. Rev. Res. **5**, 013001 (2023).

[11] C. Zhang, P. Guo, and J. Zhou, Tailoring bulk photovoltaic effects in magnetic sliding ferroelectric materials, Nano Lett. **22**, 9297 (2022).

[12] Z. Dai and A. M. Rappe, Magnetic bulk photovoltaic effect: Strong and weak field, Phys. Rev. B **107**, L201201 (2023).

[13] X. Zhou, W. Feng, R. W. Zhang, L. Smejkal, J. Sinova, Y. Mokrousov, and Y. Yao, Crystal thermal transport in altermagnetic RuO_2, Phys. Rev. Lett. **132**, 056701 (2024).

[14] S. Lee, S. Lee, S. Jung, J. Jung, D. Kim, Y. Lee, B. Seok, J. Kim, B. G. Park, L. Šmejkal, C.-J. Kang, and C. Kim, Broken Kramers degeneracy in altermagnetic MnTe, Phys. Rev. Lett. **132**, 036702 (2024).

[15] Y.-P. Zhu, X. Chen, X.-R. Liu, Y. Liu, P. Liu, H. Zha, G. Qu, C. Hong, J. Li, Z. Jiang, X.-M. Ma, Y.-J. Hao, M.-Y. Zhu, W. Liu, M. Zeng, S. Jayaram, M. Lenger, J. Ding, S. Mo, K. Tanaka, M. Arita, Z. Liu, M. Ye, D. Shen, J. Wrachtrup, Y. Huang, R.-H. He, S. Qiao, Q. Liu, and C. Liu, Observation of plaid-like spin splitting in a noncoplanar antiferromagnet, Nature (London) **626**, 523 (2024).

[16] X. Zhang, Q. Liu, J.-W. Luo, A. J. Freeman, and A. Zunger, Hidden spin polarization in inversion-symmetric bulk crystals, Nat. Phys. **10**, 387 (2014).

[17] W. Chen, M. Gu, J. Li, P. Wang, and Q. Liu, Role of hidden spin polarization in nonreciprocal transport of antiferromagnets, Phys. Rev. Lett. **129**, 276601 (2022).

[18] S. Fang, B. Wu, Q. Li, Z. Yang, H. Du, J. Yang, Z. Luo, and J. Lu, Light-assisted Néel spin currents in *PT*-symmetric antiferromagnetic semiconductors, Phys. Rev. B **109**, 085201 (2024).

[19] R.-C. Xiao, D.-F. Shao, Y.-H. Li, and H. Jiang, Spin photogalvanic effect in two-dimensional collinear antiferromagnets, npj Quantum Mater. **6**, 35 (2021).

[20] A. Manchon, H. C. Koo, J. Nitta, S. M. Frolov, and R. A. Duine, New perspectives for Rashba spin-orbit coupling, Nat. Mater. **14**, 871 (2015).

[21] B. Wu, S. Fang, J. Yang, S. Liu, Y. Peng, Q. Li, Z. Lin, J. Shi, W. Yang, Z. Luo, C. Wang, J. Yang, J. Lu, and H. Du, High-performance Fe_xGeTe_2-based ($x = 4$ or 5) van der Waals magnetic tunnel junctions, Phys. Rev. Appl. **19**, 024037 (2023).

[22] B. Wu, J. Yang, R. Quhe, S. Liu, C. Yang, Q. Li, J. Ma, Y. Peng, S. Fang, J. Shi, J. Yang, J. Lu, and H. Du, Scaling behavior of magnetoresistance with the layer number in CrI_3 magnetic tunnel junctions, Phys. Rev. Appl. **17**, 034030 (2022).

[23] J. Yang, S. Fang, Y. Peng, S. Liu, B. Wu, R. Quhe, S. Ding, C. Yang, J. Ma, B. Shi, L. Xu, X. Sun, G. Tian, C. Wang, J. Shi, J. Lu, and J. Yang, Layer-dependent giant magnetoresistance in two-dimensional $CrPS_4$ magnetic tunnel junctions, Phys. Rev. Appl. **16**, 024011 (2021).

[24] Y. Deng, Y. Yu, Y. Song, J. Zhang, N. Z. Wang, Z. Sun, Y. Yi, Y. Z. Wu, S. Wu, J. Zhu, J. Wang, X. H. Chen, and Y. Zhang, Gate-tunable room-temperature ferromagnetism in two-dimensional Fe_3GeTe_2, Nature (London) **563**, 94 (2018).

[25] J. Li, Q. Yao, L. Wu, Z. Hu, B. Gao, X. Wan, and Q. Liu, Designing light-element materials with large effective spin-orbit coupling, Nat. Commun. **13**, 919 (2022).

[26] D. Xiao, M.-C. Chang, and Q. Niu, Berry phase effects on electronic properties, Rev. Mod. Phys. **82**, 1959 (2010).

[27] J. R. Schaibley, H. Yu, G. Clark, P. Rivera, J. S. Ross, K. L. Seyler, W. Yao, and X. Xu, Valleytronics in 2D materials, Nat. Rev. Mater. **1**, 16055 (2016).

[28] Z. Luo, A. Hrabec, T. P. Dao, G. Sala, S. Finizio, J. Feng, S. Mayr, J. Raabe, P. Gambardella, and L. J. Heyderman, Current-driven magnetic domain-wall logic, Nature (London) **579**, 214 (2020).

[29] S. Datta, How we proposed the spin transistor, Nat. Electron. **1**, 604 (2018).

[30] C. Song, R. Zhang, L. Liao, Y. Zhou, X. Zhou, R. Chen, Y. You, X. Chen, and F. Pan, Spin-orbit torques: Materials, mechanisms, performances, and potential applications, Prog. Mater. Sci. **118**, 100761 (2021).

[31] D. Niesner, M. Wilhelm, I. Levchuk, A. Osvet, S. Shrestha, M. Batentschuk, C. Brabec, and T. Fauster, Giant rashba splitting in $CH_3NH_3PbBr_3$ organic-inorganic perovskite, Phys. Rev. Lett. **117**, 126401 (2016).

[32] A. K. Jena, A. Kulkarni, and T. Miyasaka, Halide perovskite photovoltaics: background, status, and future prospects, Chem. Rev. **119**, 3036 (2019).

[33] M. Wu, Two-Dimensional van der waals ferroelectrics: Scientific and technological opportunities, ACS Nano **15**, 9229 (2021).

[34] L. Qi, S. Ruan, and Y. J. Zeng, Review on recent developments in 2D ferroelectrics: Theories and applications, Adv. Mater. **33**, e2005098 (2021).

[35] H. Sun, J. Gu, Y. Li, T. R. Paudel, D. Liu, J. Wang, Y. Zang, C. Gu, J. Yang, W. Sun, Z. Gu, E. Y. Tsymbal, J. Liu, H. Huang, D. Wu, and Y. Nie, Prominent size effects without a depolarization field observed in ultrathin ferroelectric oxide membranes, Phys. Rev. Lett. **130**, 126801 (2023).

[36] S. Fang, C. Yang, Q. Li, B. Wu, L. Xu, S. Liu, J. Yang, J. Ma, J. Dong, Y. Li, J. Yang, and J. Lu, Ferroelectric-Tunable photoresponse in α-In_2Se_3 photovoltaic photodetectors: An *ab initio* quantum transport study, Phys. Rev. Appl. **19**, 024024 (2023).

[37] D. Zhang, P. Schoenherr, P. Sharma, and J. Seidel, Ferroelectric order in van der waals layered materials, Nat. Rev. Mater. **8**, 25 (2022).

[38] S. Fang, Q. Li, C. Yang, B. Wu, S. Liu, J. Yang, J. Ma, Z. Yang, K. Tang, and J. Lu, Polarization tunable bidirectional photoresponse in Van der Waals α-In_2Se_3/NbX_2 (X = S, Se, and Te) ferroelectric diodes, Phys. Rev. Mater. **7**, 084412 (2023).

[39] M. Fang, Y. Wang, H. Wang, Y. Hou, E. Vetter, Y. Kou, W. Yang, L. Yin, Z. Xiao, Z. Li, L. Jiang, H. N. Lee, S. Zhang, R. Wu, X. Xu, D. Sun, and J. Shen, Tuning the interfacial spin-orbit coupling with ferroelectricity, Nat. Commun. **11**, 2627 (2020).

[40] U. Schroeder, M. H. Park, T. Mikolajick, and C. S. Hwang, The fundamentals and applications of ferroelectric HfO_2, Nat. Rev. Mater. **7**, 653 (2022).

[41] J. Chen, K. Wu, W. Hu, and J. Yang, Spin-Orbit coupling in 2D semiconductors: A theoretical perspective, J. Phys. Chem. Lett. **12**, 12256 (2021).

[42] J. Gou, H. Bai, X. Zhang, Y. L. Huang, S. Duan, A. Ariando, S. A. Yang, L. Chen, Y. Lu, and A. T. S. Wee, Two-dimensional ferroelectricity in a single-element bismuth monolayer, Nature (London) **617**, 67 (2023).

[43] J. P. Perdew, K. Burke, and M. Ernzerhof, Generalized gradient approximation made simple, Phys. Rev. Lett. **77**, 3865 (1996).

[44] G. Kresse and D. Joubert, From ultrasoft pseudopotentials to the projector augmented-wave method, Phys. Rev. B **59**, 1758 (1999).

[45] P. E. Blochl, Projector augmented-wave method, Phys. Rev. B **50**, 17953 (1994).

[46] G. Kresse and J. Hafner, *Ab initio* molecular dynamics for open-shell transition metals, Phys. Rev. B **48**, 13115 (1993).

[47] V. Wang, N. Xu, J.-C. Liu, G. Tang, and W.-T. Geng, VASPKIT: A user-friendly interface facilitating high-throughput computing and analysis using VASP code, Comput. Phys. Commun. **267**, 108033 (2021).

[48] H.-J. Kim, C. Li, J. Feng, J.-H. Cho, and Z. Zhang, Competing magnetic orderings and tunable topological states in two-dimensional hexagonal organometallic lattices, Phys. Rev. B **93**, 041404(R) (2016).

[49] J. Chen, Y. Hu, and H. Guo, First-principles analysis of photocurrent in graphene *P N* junctions, Phys. Rev. B **85**, 155441 (2012).

[50] M. Brandbyge, J.-L. Mozos, P. Ordejón, J. Taylor, and K. Stokbro, Density-functional method for nonequilibrium electron transport, Phys. Rev. B **65**, 165401 (2002).

[51] J. Taylor, H. Guo, and J. Wang, *Ab initio* modeling of quantum transport properties of molecular electronic devices, Phys. Rev. B **63**, 245407 (2001).

[52] S. Smidstrup, T. Markussen, P. Vancraeyveld, J. Wellendorff, J. Schneider, T. Gunst, B. Verstichel, D. Stradi, P. A. Khomyakov, U. G. Vej-Hansen, M. E. Lee, S. T. Chill, F. Rasmussen, G. Penazzi, F. Corsetti, A. Ojanpera, K. Jensen, M. L. N. Palsgaard, U. Martinez, A. Blom, M. Brandbyge, and K. Stokbro, QuantumATK: An integrated platform of electronic and atomic-scale modelling tools, J. Phys.: Condens. Matter **32**, 015901 (2020).

[53] L. Kleinman and D. M. Bylander, Efficacious form for model pseudopotentials, Phys. Rev. Lett. **48**, 1425 (1982).

[54] L. Zhang, K. Gong, J. Chen, L. Liu, Y. Zhu, D. Xiao, and H. Guo, Generation and transport of valley-polarized current in transition-metal dichalcogenides, Phys. Rev. B **90**, 195428 (2014).

[55] B. Wu, J. Yang, S. Liu, S. Fang, Z. Liu, Z. Lin, J. Shi, W. Yang, Z. Luo, C. Wang, H. Du, J. Yang, and J. Lu, Layer-Dependent magnetoresistance and spin-transfer torque in $MnSe_2$-Based magnetic tunnel junctions, Phys. Rev. Appl. **19**, 064008 (2023).

[56] M. Long, P. Wang, H. Fang, and W. Hu, Progress, challenges, and opportunities for 2D material based photodetectors, Adv. Funct. Mater. **29**, 1803807 (2018).

[57] J. Ji, G. Yu, C. Xu, and H. J. Xiang, General theory for bilayer stacking ferroelectricity, Phys. Rev. Lett. **130**, 146801 (2023).

[58] F. Freimuth, S. Blügel, and Y. Mokrousov, Charge and spin photocurrents in the Rashba model, Phys. Rev. B **103**, 075428 (2021).

[59] C. Yang, Z. Song, X. Sun, and J. Lu, Valley pseudospin in monolayer $MoSi_2N_4$ and $MoSi_2As_4$, Phys. Rev. B **103**, 035308 (2021).

[60] A. Manchon, J. Železný, I. M. Miron, T. Jungwirth, J. Sinova, A. Thiaville, K. Garello, and P. Gambardella, Current-induced spin-orbit torques in ferromagnetic and antiferromagnetic systems, Rev. Mod. Phys. **91**, 035004 (2019).

[61] X. Cartoixà, L. W. Wang, D. Z. Y. Ting, and Y. C. Chang, Higher-order contributions to Rashba and Dresselhaus effects, Phys. Rev. B **73**, 205341 (2006).

[62] R. Fei, W. Kang, and L. Yang, Ferroelectricity and phase transitions in monolayer Group-IV monochalcogenides, Phys. Rev. Lett. **117**, 097601 (2016).

[63] K. Chang, J. Liu, H. Lin, N. Wang, K. Zhao, A. Zhang, F. Jin, Y. Zhong, X. Hu, W. Duan, Q. Zhang, L. Fu, Q.-K. Xue, X. Chen, and S.-H. Ji, Discovery of robust in-plane ferroelectricity in atomic-thick SnTe, Science **353**, 274 (2016).

[64] S. Zhong, X. Zhang, S. Liu, S. A. Yang, and Y. Lu, Giant and nonanalytic negative piezoelectric response in elemental Group-Va ferroelectric monolayers, Phys. Rev. Lett. **131**, 236801 (2023).

[65] X. Zhao, K. Song, H. Huang, W. Han, and Y. Yang, Ferroelectric materials for solar energy scavenging and photodetectors, Adv. Opt. Mater. **10**, 2101741 (2021).

[66] X. Han, Y. Ji, and Y. Yang, Ferroelectric photovoltaic materials and devices, Adv. Funct. Mater. **32**, 2109625 (2021).

[67] B. Xu, H. Xiang, Y. Xia, K. Jiang, X. Wan, J. He, J. Yin, and Z. Liu, Monolayer $AgBiP_2Se_6$: An atomically thin ferroelectric semiconductor with out-plane polarization, Nanoscale **9**, 8427 (2017).

[68] S. Yuan, X. Luo, H. L. Chan, C. Xiao, Y. Dai, M. Xie, and J. Hao, Room-temperature ferroelectricity in $MoTe_2$ down to the atomic monolayer limit, Nat. Commun. **10**, 1775 (2019).

[69] F. Liu, L. You, K. L. Seyler, X. Li, P. Yu, J. Lin, X. Wang, J. Zhou, H. Wang, H. He, S. T. Pantelides, W. Zhou, P. Sharma, X. Xu, P. M. Ajayan, J. Wang, and Z. Liu, Room-temperature ferroelectricity in $CuInP_2S_6$ ultrathin flakes, Nat. Commun. **7**, 12357 (2016).

[70] A. Dziaugys, K. Kelley, J. A. Brehm, L. Tao, A. Puretzky, T. Feng, A. O'Hara, S. Neumayer, M. Chyasnavichyus, E. A. Eliseev, J. Banys, Y. Vysochanskii, F. Ye, B. C. Chakoumakos, M. A. Susner, M. A. McGuire, S. V. Kalinin, P. Ganesh, N. Balke, S. T. Pantelides, A. N. Morozovska, and P. Maksymovych, Piezoelectric domain walls in van der Waals antiferroelectric $CuInP_2Se_6$, Nat. Commun. **11**, 3623 (2020).

[71] R. Fei and L. Yang, Room-temperature ferroelectric switching, Nat. Electron. **4**, 703 (2021).

[72] M. Vizner Stern, Y. Waschitz, W. Cao, I. Nevo, K. Watanabe, T. Taniguchi, E. Sela, M. Urbakh, O. Hod, and M. Ben Shalom, Interfacial ferroelectricity by van der Waals sliding, Science **372**, 1462 (2021).

[73] K. Yasuda, X. Wang, K. Watanabe, T. Taniguchi, and P. Jarillo-Herrero, Stacking-engineered ferroelectricity in bilayer boron nitride, Science **372**, 1458 (2021).

[74] Z. Fei, W. Zhao, T. A. Palomaki, B. Sun, M. K. Miller, Z. Zhao, J. Yan, X. Xu, and D. H. Cobden, Ferroelectric switching of a two-dimensional metal, Nature (London) **560**, 336 (2018).

[75] Q. He, Z. Tang, M. Dai, H. Shan, H. Yang, Y. Zhang, and X. Luo, Epitaxial growth of large area two-dimensional ferroelectric alpha-In$_2$Se$_3$, Nano Lett. **23**, 3098 (2023).

[76] Z. Dai, A. M. Schankler, L. Gao, L. Z. Tan, and A. M. Rappe, Phonon-assisted ballistic current from first-principles calculations, Phys. Rev. Lett. **126**, 177403 (2021).

[77] See Supplemental Material at http://link.aps.org/supplemental/10.1103/PhysRevB.109.195202 for details of the comparison between the nonequilibrium Green's function (NEGF) method and high-order perturbation theory, Temperatures in the NEGF method and density functional theory, spin photogalvanic effect under left-handed circularly-polarized light of BP-Bi and α-GeTe, and spin texture of the second valence band of BP-Bi, and it includes Ref. [78].

[78] Z. Song, X. Sun, and L.-W. Wang, Eshelby-twisted three-dimensional moiré superlattices, Phys. Rev. B **103**, 245206 (2021).

[79] S. Varotto, L. Nessi, S. Cecchi, J. Sławińska, P. Noël, S. Petrò, F. Fagiani, A. Novati, M. Cantoni, D. Petti, E. Albisetti, M. Costa, R. Calarco, M. Buongiorno Nardelli, M. Bibes, S. Picozzi, J.-P. Attané, L. Vila, R. Bertacco, and C. Rinaldi, Room-temperature ferroelectric switching of spin-to-charge conversion in germanium telluride, Nat. Electron. **4**, 740 (2021).

[80] M. Si, A. K. Saha, S. Gao, G. Qiu, J. Qin, Y. Duan, J. Jian, C. Niu, H. Wang, W. Wu, S. K. Gupta, and P. D. Ye, A ferroelectric semiconductor field-effect transistor, Nat. Electron. **2**, 580 (2019).

[81] J. Chen, Y. Zhou, J. Yan, J. Liu, L. Xu, J. Wang, T. Wan, Y. He, W. Zhang, and Y. Chai, Room-temperature valley transistors for low-power neuromorphic computing, Nat. Commun. **13**, 7758 (2022).

[82] W. Han, X. Zheng, K. Yang, C. S. Tsang, F. Zheng, L. W. Wong, K. H. Lai, T. Yang, Q. Wei, M. Li, W. F. Io, F. Guo, Y. Cai, N. Wang, J. Hao, S. P. Lau, C. S. Lee, T. H. Ly, M. Yang, and J. Zhao, Phase-controllable large-area two-dimensional In$_2$Se$_3$ and ferroelectric heterophase junction, Nat. Nanotechnol. **18**, 55 (2023).